



UNIVERSITY OF LEEDS

This is a repository copy of *Variations of hydraulic properties of granular sandstones during water inrush: effect of small particle migration*.

White Rose Research Online URL for this paper:
<http://eprints.whiterose.ac.uk/109856/>

Version: Accepted Version

Article:

Ma, D, Rezania, M, Yu, H-S et al. (1 more author) (2017) Variations of hydraulic properties of granular sandstones during water inrush: effect of small particle migration. *Engineering Geology*, 217. pp. 61-70. ISSN 0013-7952

<https://doi.org/10.1016/j.enggeo.2016.12.006>

© 2016 Elsevier B.V. Licensed under the Creative Commons Attribution-NonCommercial-NoDerivatives 4.0 International
<http://creativecommons.org/licenses/by-nc-nd/4.0/>

Reuse

Unless indicated otherwise, fulltext items are protected by copyright with all rights reserved. The copyright exception in section 29 of the Copyright, Designs and Patents Act 1988 allows the making of a single copy solely for the purpose of non-commercial research or private study within the limits of fair dealing. The publisher or other rights-holder may allow further reproduction and re-use of this version - refer to the White Rose Research Online record for this item. Where records identify the publisher as the copyright holder, users can verify any specific terms of use on the publisher's website.

Takedown

If you consider content in White Rose Research Online to be in breach of UK law, please notify us by emailing eprints@whiterose.ac.uk including the URL of the record and the reason for the withdrawal request.



eprints@whiterose.ac.uk
<https://eprints.whiterose.ac.uk/>

Accepted Manuscript

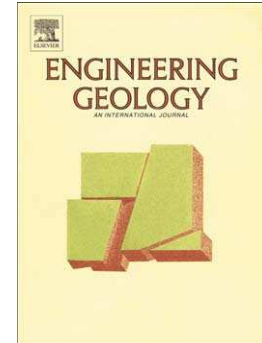
Variations of hydraulic properties of granular sandstones during water inrush:
effect of small particle migration

Dan Ma, Mohammad Rezaia, Hai-Sui Yu, Hai-Bo Bai

PII: S0013-7952(16)30810-9
DOI: doi:[10.1016/j.enggeo.2016.12.006](https://doi.org/10.1016/j.enggeo.2016.12.006)
Reference: ENGEO 4436

To appear in: *Engineering Geology*

Received date: 5 August 2016
Revised date: 11 December 2016
Accepted date: 15 December 2016



Please cite this article as: Ma, Dan, Rezaia, Mohammad, Yu, Hai-Sui, Bai, Hai-Bo, Variations of hydraulic properties of granular sandstones during water inrush: effect of small particle migration, *Engineering Geology* (2016), doi:[10.1016/j.enggeo.2016.12.006](https://doi.org/10.1016/j.enggeo.2016.12.006)

This is a PDF file of an unedited manuscript that has been accepted for publication. As a service to our customers we are providing this early version of the manuscript. The manuscript will undergo copyediting, typesetting, and review of the resulting proof before it is published in its final form. Please note that during the production process errors may be discovered which could affect the content, and all legal disclaimers that apply to the journal pertain.

Variations of hydraulic properties of granular sandstones during water inrush: effect of small particle migration

Dan Ma^{1,2}, Mohammad Rezania^{3,*}, Hai-Sui Yu⁴, Hai-Bo Bai¹

1. State Key Laboratory for Geomechanics and Deep Underground Engineering, China
University of Mining and Technology, Xuzhou 221116, Jiangsu, China
2. Nottingham Centre for Geomechanics, Faculty of Engineering, University of Nottingham,
Nottingham NG7 2RD, UK
3. School of Engineering, University of Warwick, Coventry CV4 7AL, UK (formerly:
Nottingham Centre for Geomechanics, Faculty of Engineering, University of Nottingham,
Nottingham NG7 2RD, UK)
4. School of Civil Engineering, University of Leeds, Leeds LS2 9JT, UK

*Corresponding author

Email addresses:

Dan Ma, madan518@126.com, dan.ma@nottingham.ac.uk

Mohammad Rezania, rezaniam@yahoo.com, m.rezania@warwick.ac.uk

Hai-Sui Yu, h.yu@leeds.ac.uk

Hai-Bo Bai, hbbaicumt@126.com

Abstract

The evaluation of the hydraulic properties evolution of granular sandstones in relation with groundwater inrush within faults is an important issue for mining engineering applications. This paper presents the results of an experimental investigation of small particle migration from granular sandstone samples under different original porosities, particle size compositions and water flow pressures. A new rock testing system has been setup to carry out the tests. Based on the results, it is observed that the overall permeability evolution during the tests can be divided into four different phases, including i) re-arrangement of large rock fragments, ii) water inrush with substantial particle migration, iii) continued moderate particles seepage, and iv) steady state water flow. The crushing of edges and corners of large rock fragments, and the evolution of the fracture network has mainly been observed in the first two phases of the tests. The results indicate that the migration of small particles has an essential effect on permeability and porosity increase during water inrush through fractured sandstone. The samples with higher original porosity, higher percentage of fine particles in their formation and under higher water flow pressures, achieve higher permeability and porosity values when the test is complete. Furthermore, using the measured data, the performances of a number of empirical models, for permeability evolution in fractured porous media, have been studied. The prediction results indicate that not all of the fractures in a sample domain contribute in small particle migration. There are parts of the fracture network that are not effective in particle flow, a sample with less original porosity, more fine particles and under lower water pressure shows less ineffective fractures. Therefore, using the concept of the effective porosity (fracture) is sufficient enough for the flow calculation.

Keywords: granular sandstone; groundwater inrush; particle migration; permeability; porosity.

List of Symbols

d	particle size [L]
\bar{d}	percentage remaining for particles with size 2.5~10 mm [-]
$\bar{\bar{d}}$	percentage remaining for particles with size 2.5~15 mm [-]
h_s	height of the sample before loading [L]
h_0	height of the sample after loading [L]
H_1	height of the cylindrical tube [L]
H_2	pedestal thickness [L]
H_3	porous plate thickness [L]
H_4	filter pad thickness [L]
H_5	water flushing cap thickness [L]
H_6	height of the outflow regulator inside the cylindrical tube [L]
H_7	height of the outflow regulator [L]
H_8	height of the outflow regulator exceeding the cylindrical tube [L]
m_s	mass of the sample [M]
p	water pressure [$ML^{-1}T^{-2}$]
p_a	water pressure at the intake boundary [$ML^{-1}T^{-2}$]
p_b	water pressure connected with atmosphere [$ML^{-1}T^{-2}$]
R^2	coefficient of determination [-]
r	radius of the sample container [L]
t	time [T]
v	water flow velocity [LT^{-1}]
z	vertical axis going through the center of the sample [L]
Δ	partial differential operator [-]
$\Delta()/\Delta z$	Nabla operator [L^{-1}]
μ_w	water kinetic viscosity [$ML^{-1}T^{-1}$]
ϕ	porosity [-]
ϕ_s	porosity of the sample before loading [-]
ϕ_0	porosity of the sample after loading and before water flow initiation [-]
κ	permeability [L^2]
κ_0	permeability of the sample after loading and before water flow initiation [L^2]
ρ_s	mass density [ML^{-3}]
ρ_w	water density [ML^{-3}]

1. Introduction

China, after Russia and the United States, has the largest proven reserves of coal in the world, it is currently the world's largest coal producer (Miao and Qian, 2009). Currently, coal accounts for 70 percent of China's primary energy production; therefore, China's economic development during the foreseeable future will still be highly dependent on coal extraction and production. The extraction of this important resource is often associated with groundwater inrush accidents. Indeed, more than 90% of the casualties in mining work accidents in China are due to water inflow from karst aquifers into the mine through the floor of the coal seam (Li and Zhou, 2006). According to recent statistics (State Administration of Coal Mine Safety, 2014), during the 2000's, groundwater inrush accidents in Chinese mines resulted in the death of several hundred miners each year; although since mid 2000's with increasing application of groundwater inrush prevention systems, the number of related coal mine accidents has shown a clear descending trend (Sun et al., 2016).

In addition to threatening the safety of mining operations, groundwater inrush also causes pollution due to mine spillage (Li and Zhou, 2006; Wu and Zhou, 2008; Zhu and Wei, 2011). Therefore, over the past few years, field and laboratory investigations of the effects of groundwater inrush on hydraulic and mechanical properties of rocks (Bai et al., 2013), and consequently mining environment (Bai and Miao, 2016), have been carried out extensively (e.g., Wu and Zhou, 2008; Ma et al., 2015a). The results from these investigations show that high pressure groundwater can break through the reduced stress zones around the mining face and leak into the working areas which can potentially trigger the hazardous water inrush incident (Li et al., 2011; Miao et al., 2011a). The characteristics of confined aquifer, combined with the mining-induced strata failure (Meng et al., 2016) and the inherent geological structures of the field (Huang et al., 2016), such as water conducting faults, are among the main factors that set off such events (Li and Zhou, 2006; Li et al., 2011; Wu and Zhou, 2008; Zhang et al., 2014; Zhu et al., 2013; Zhu and Wei, 2011). As shown in

Fig. 1, the fault fracture zones that contain lots of granular rock fragments can act as effective water inrush channels. It can be argued that the existence of small particles within the faults and voids could be a controlling factor in determining the safety of coal mining activities above confined aquifers (Lu and Wang, 2015; Li et al., 2015; Lu et al., 2015; Ma et al., 2016a).

Up to now, the studies on groundwater inrush mechanism have been mainly concentrated on either the reaction of faults or the damage of floor strata (Caine et al., 1996; Babiker and Gudmundsson, 2004; Zhu and Wei, 2011). Potentially influential aspects, such as the configurational structure of particles within the crushed rock zone and the variations of hydraulic properties have been mainly overlooked in the past studies of the faults (Zhang et al., 2016). A number of researchers have studied the effect of fluid flow on particle rearrangements within a granular setting and have reported strong permeability variation (e.g., Miao et al., 2004, 2011b; Johnsen et al., 2007, 2008; Niebling et al., 2012; Ma et al., 2015b, 2016b). Therefore, in addition to the factors such as the geological features of the mining fields (Rutter et al., 2013; Zhang et al., 2014), groundwater condition and extraction percentage of mines (Blodgett and Kuipers, 2002; Booth, 2006), it is also a significant issue to consider the hydraulic properties of granular rocks within the faults.

This paper aims to study the effects of small particle migration on the mechanism of mining-induced water inrush within faults. To carry out the investigation, a new experimental system has been set up, which is capable of quantifying the influence of varying porosity, particle size composition and water pressure on the hydraulic properties of granular sandstones. In the following the details of the testing system and conducted experiments are explained.

2. Experimental Details

2.1. Testing equipment

As shown in Fig. 2, the experimental system for testing small particle migration within fractured rocks is comprising of five different parts: (a) rock particle flow testing cell and frame, (b) water

pressure control equipment, (c) sample porosity control device, (d) automatic data acquisition and storage system and (e) rock particle collection module. Further details of each part of the testing system are explained in the following.

- (a) The key component of this experimental system is the in-house made rock particle flow equipment (Fig. 3), which is mainly made up of a cylindrical sample container, an overflow tank, a water flushing cap and an outflow regulator. The main feature of the designed system is that it allows small particles to migrate out of the sample container under water pressure. Fig. 3(a) shows the schematics of the main components of the designed system. The loading ram (no. 1 in Fig. 3(a)) at the top of the sample container is used to apply vertical pressure on the sample in order to alter its porosity. The porosity variation is controlled by the sample porosity control device (Fig. 2c), that applies displacement to the sample from its bottom boundary. The over flow tank (no. 3 in Fig. 3(a)) is fixed to the cylindrical sample container (no. 6 in Fig. 3(a)) using the bolts (nos. 5 and 12 in Fig. 3(a)). The cylindrical sample container cell (no. 6 in Fig. 3(a)) is sealed to the pedestal (no. 8 in Fig. 3(a)) at the bottom by rubber O-rings (no. 7 in Fig. 3(a)). The porous metal disk (no. 9 in Fig. 3(a)), with uniformly distributed holes, ensures that the water flows evenly; furthermore, the filter pad (no. 10 in Fig. 3(a)) at the bottom of the sample captures the small sandstone particles so that the porous metal disk (no. 9 in Fig. 3(a)) is not blocked. The particular design of the water flushing cap (no. 13 in Fig. 3(a)), at the top of the sample, together with the outflow regulator (no. 14 in Fig. 3(a)), ensure that the small rock particles with a diameter of less than 10 mm can be washed out of the sample medium and are not thrown out of the overflow tank. Moreover, the water flushing cap and the outflow regulator can prevent the sideslip of overflow tank cover (no. 2 in Fig. 3(a)) that ensures stable loading and uniform compression of the sandstone samples.

- (b) The water pressure control equipment shown in Fig. 2(b) is made up of a water pump and a relief valve, which can supply a constant and stable water pressure to the sample. During the test the water pump is used to fill the hydraulic cylinder with water and then, using the oil pump, the water is flushed into the sample with a constant flow pressure.
- (c) The porosity control device (Fig. 2c) includes a hydraulic cylinder, a displacement sensor and an oil pump. To replicate different compression levels, a compressive pressure is applied by means of the oil pump and the hydraulic cylinder, then the sample height is measured by a displacement sensor; therefore, the corresponding porosity of the sample can be calculated.
- (d) A water pressure transducer, a flow rate sensor and data logger and a personal computer are the main components of the automatic data acquisition and storage system (Fig. 2d), which is mainly used to collect the water pressure and flow velocity data.
- (e) The small particle collection module (Fig. 2e) is made up of fine gauze and vibrosieve, which is used to collect and filter the small particles mixed with the water flow.

2.2. Sandstone specimens description

According to the field investigations in Buliangou mining area of Zhungeer coalfield in Inner Mongolia of China, the geological condition of the area is mainly composed of a mixture of small rock particles and large rock masses (see Fig. 4). X-ray diffraction analysis tests (BGMRE, 2006) show that the sandstone component content of the in-situ rock is high. Therefore, sandstone rock blocks, taken from a depth of approximately 300 m from the abovementioned mining area, are used as testing material for this study. In the laboratory, the sandstone specimens have been crushed into particles smaller than 20 mm. The crushing of sandstone blocks has been done in two steps. Firstly, the sandstone blocks are hammered into pieces of 60 mm, or less, in diameter using steel piercers and iron hammers. Then, a special stone crusher is used to crush those large pieces into grains with sizes

less than 20 mm in diameter. Thereafter, using a vibratory sieve shaker, the crushed sandstone grains are separated into four groups with different particle size ranges of: 2.5–5 mm, 5–10 mm, 10–15 mm and 15–20 mm (see Fig. 5 for particle size of 15–20 mm as an example).

For the experiments, the grain sizes of 0–5 mm and 5–10 mm, mixed with a weight ratio of 1:1, are defined as the small rock particles, and grain sizes of 10–15 mm and 15–20 mm, mixed with a weight ratio of 1:1 are considered as the main (large) rock fragments. The testing samples are prepared by small rock particles and main rock fragments combined with weight ratios of 1:2 (sample A), 1:1 (sample B) and 2:1 (sample C). Therefore, the testing samples are constituted of different grain sizes with weight ratios of 1:1:2:2 for sample A, 1:1:1:1 for sample B, and 2:2:1:1 for sample C. Each sample weighs 1800 g.

2.3. Experimental procedure

The experiments are carried out at room temperature, the testing fluid is water with kinetic viscosity $\mu_w = 1.01 \times 10^{-3}$ Pa·s and density $\rho_w = 1000$ kg/m³. Before each experiment, the sandstone samples are completely saturated with water. Each sample is tested three times for higher reliability of the measurements; the final result is taken as the average value from the three tests. The tests are conducted at different porosities, particle size distributions and water pressures, as summarized in the following

- In terms of porosity, sample B at constant water pressure of 0.7 MPa, is tested at different heights of 110, 120 and 130 mm, with corresponding porosities of 0.288, 0.348 and 0.398.
- In terms of particle size distribution, at constant water pressure of 0.7 MPa and similar sample height of 120 mm, three different samples A, B, and C are tested (with different particle size weight ratios).
- In terms of water pressure, sample B at the same porosity (i.e., 120 mm sample height), is tested at three different pressures of 0.4, 0.7 and 1 MPa.

The details of each sample composition are summarized in Table 1. For each experiment the washed away particles are collected every 20 seconds, and the overall duration of the test is 160 seconds.

2.4. Measurement of hydraulic properties

Within the setting of the experimental system detailed in previous section, water flow flushes the small particles out of the sandstone samples, which consequently results in the increase of permeability and porosity of the samples. Based on the rate of particle migration, the permeability and porosity increase rates of the samples can be evaluated as discussed in the following.

2.4.1. Permeability

To quantify the permeability evolution of the granular sandstone samples, the one-dimensional Darcy equation could be used as:

$$-\Delta p / \Delta z = \mu_w v \kappa^{-1} \quad (1)$$

where $\Delta p / \Delta z$ is the pore pressure gradient; z is the dimensional variable; μ_w is the water viscosity; κ is the permeability of the sample medium; v is average water flow velocity which is calculated by the radius of cylindrical container r and water flow rate Q as $v = Q / (\pi r^2)$. In an incremental manner, the permeability can be calculated for each time interval t_i (where $i = 1 \dots n$). Therefore, Eq. (1) can be rewritten as:

$$-\Delta p_i / \Delta z_i = \mu_w v_i \kappa_i^{-1} \quad (2)$$

For the tests, the bottom end of the sample is connected to the water pressure control equipment of the testing system that automatically records water pressure changes Δp_i over time t_i . The top end of the sample is connected with the atmosphere, resulting in an atmospheric pressure boundary p_{bi} equal to zero. The steady state value of pore water pressure at the intake boundary at time t_i is

assumed to be p_{ai} , and with the water pressure not changing at the intake boundary during the time interval t_i , p_{ai} could be considered equal to p . Furthermore, the height of the sample h_0 is kept unchanged during the water flow. Therefore, the incremental water pressure gradient $\Delta p_i / \Delta z_i$ can be considered as $\Delta p / \Delta z$, which is unchanged and could be determined by water pressure difference at the two boundaries of the sample, as:

$$\Delta p_i / \Delta z_i = -(p_{ai} - p_{bi}) / h_0 = -p_{ai} / h_0 = -p / h_0 \quad (3)$$

The one-dimensional flow direction is vertically upward, therefore the incremental permeability κ_i at time t_i can be obtained as:

$$\kappa_i = \mu_w v_i h_0 / p \quad (4)$$

2.4.2. Porosity

Porosity is a crucial factor to describe the hydraulic properties of granular sandstones. For these tests, the values of porosity before the application of load (i.e., axial displacement), and after the application of load (just before the water flow initiation) are calculated. The evolution of porosity during the water flow is also measured.

- Porosity before the application of load

At the first stage, the granular sandstone sample, with a mass m_s of 1800 g, is placed into the sample container and the loading ram is lowered to preliminarily compress the sample. The porosity ϕ_s at this stage can be expressed as:

$$\phi_s = 1 - m_s / (\pi r^2 \rho_s h_s) \quad (5)$$

where ρ_s is the density of the sandstone sample, r is the radius of the cylindrical container, and h_s is the height of the sample. As shown in Fig. 6, considering the height of the cylindrical container H_1

(180 mm), the pedestal thickness H_2 (25 mm), the porous plate thickness H_3 (10 mm), the filter pad thickness H_4 (2 mm), the water flushing cap thickness H_5 (20 mm), and the height of the outflow regulator that intrudes the cylindrical tube H_6 , the height of the sample h_s can be calculated as:

$$h_s = H_1 - (H_2 + H_3 + H_4 + H_5 + H_6) \quad (6)$$

As H_1, H_2, H_3 and H_4 have all been set when the testing system was designed, h_s could be only related to H_6 . The height H_6 can be evaluated by subtracting the height of the outflow regulator exceeding the cylindrical tube H_8 , from the total height of the outflow regulator H_7 (75 mm)

$$H_6 = H_7 - H_8 \quad (7)$$

A displacement sensor could be used to measure H_8 ; therefore, the sample height h_s before the application of load is

$$h_s = (H_1 + H_8) - (H_2 + H_3 + H_4 + H_5 + H_7) = H_8 + 180 - (25 + 10 + 2 + 20 + 75) = H_8 + 48 \quad (8)$$

Consequently, Eq. (5), for the calculation of porosity, can be rewritten as:

$$\phi_s = 1 - m_s / [\pi r^2 \rho_s (H_8 + 48)] \quad (9)$$

- Original porosity after load application and before water flow

Before the initiation of water flow through the sample, an axial displacement is applied to compress the sample by Δh . Given the reduced initial sample height of $h_0 = h_s - \Delta h$, the so-called original porosity ϕ_0 of the sample at this stage can be calculated as:

$$\phi_0 = 1 - m_s / (\pi r^2 \rho_s h_0) = 1 - m_s / [\pi r^2 \rho_s (H_8 - \Delta h + 48)] \quad (10)$$

- Porosity evolution during water flow

During the test, the washed away particles are collected every 20 seconds (Δt), and the masses measured at the time intervals read Δm_{t_1} , Δm_{t_2} ... Δm_{t_n} . As the duration of each test is 160 seconds, the maximum n value is 8. The total collected mass m_j for $t_j = j \cdot \Delta t$ ($j = 1, 2, \dots, n$), and the average mass migration rate m'_j during any time interval can, respectively, be calculated as:

$$m_j = \Delta m_{t_1} + \Delta m_{t_2} + \dots + \Delta m_{t_j} \quad (j = 1, 2, \dots, n) \quad (11)$$

$$m'_j = \Delta m_j / \Delta t \quad (j = 1, 2, \dots, n) \quad (12)$$

The migration of small particles will result in the increase of porosity. The porosity ϕ_j at a specific time t_j , and the porosity increase rate ϕ'_j during any time interval can, respectively, be calculated by:

$$\phi_j = \phi_0 + m_j / (\pi r^2 \rho_s h_0) = \phi_0 + (\Delta m_{t_1} + \Delta m_{t_2} + \dots + \Delta m_{t_j}) / (\pi r^2 \rho_s h_0) \quad (j = 1, 2, \dots, n) \quad (13)$$

$$\phi'_j = (\phi_j - \phi_{t(j-1)}) / \Delta t \quad (j = 1, 2, \dots, n) \quad (14)$$

3. Results and discussions

3.1. The evolution of hydraulic properties

For each test, the evolution of permeability is calculated based on Eq. (4) and using an average value of water flow velocity v_i for the respective t_i ($i = 1 \dots n$). The results for the permeability evolution are shown in Fig. 7. At every 20 seconds, based on the cumulative mass of migrated particles (see Eq. (11)), using Eq. (13) the value of sample porosity can be obtained. Furthermore, using Eqs. (12) and (14), for every time interval the average weight migration rate and the porosity increase rate can be calculated. Figs. 8(a) and (b) show, for different samples, the variations of porosity and the porosity increase rate with time, respectively.

According to the experimental observations, the permeability and porosity changes settle after about 120 seconds from when the maximum rate of variations occurs (see Fig. 8(b)). Based on the

results illustrated in Fig. 7, the overall process of permeability evolution during the tests can be divided into four different phases. These phases, which are explained in the sequel, include adjustment of rock fragments, water inrush with substantial particle migration, continued moderate particle migration, and steady state water flow.

The first phase involves the adjustment of large rock fragments during which the sandstone sample configuration is changing due to the rearrangements of larger grains. Although, generally at this stage the permeability is increasing; however, in almost all the tests the permeability increase trend includes notable fluctuations. This is due to the fact that the large grains, in their pursuit of a stable reconfiguration under water flow, are forming a number of less stable intermediate arrangements. This can also be attributed to the crushing of corners and edges of large grains during their rearrangements that result in new and random fracture channels. At this phase the water flows are found to be slightly turbid, and almost no apparent migration of small particles out of the samples is observed. Furthermore, during this first stage all samples experience the maximum rate of porosity increase (see Fig. 8(b)).

The second stage involves a water inrush phase through the sample, during which in a very short time the water flow velocity increases rapidly. During this phase, it is observed that, under the effect of increased flow velocity, major channels for flow and particle migration are forming inside the sample medium, and as a result maximum amounts of small particles are eroded out of the samples. The permeability increase at this stage, for all the tests, is found to be significant and rapid; however, there are still a number of abrupt fluctuations within their (generally increasing) trends.

The third phase of permeability evolution involves continuous, but moderate, discharge of small particles out of the samples. During this stage, significantly fewer particles continue to migrate out of the samples through the flow channels that have been formed in the last stage. Also, as the pace of

particle migration is becoming particularly slower in this phase, that results in milder increase of permeability and porosity during this stage.

The flow experiments are carried out until steady state flow condition is reached, i.e., the water flow rate stabilizes at outflow tank. At this final phase of the experiments, there are no more small particles migrating out of the samples, and the permeability and porosity values generally remain constant.

It should be noted that in this study, given the designed experimental setup, the granular sandstone samples were not looked at as dual-domain systems investigating the separate effects of permeability variations within the 1) fragments and 2) fracture networks. Indeed, the porosity and permeability changes through individual sandstone lumps and fragments may contribute to the overall variations of hydraulic properties within sandstone samples, but investigating it would require a more sophisticated testing equipment considering that during the tests some large particles also break into smaller ones. Therefore, in this research the overall variations of the hydraulic properties within the domain, as a whole, under water inrush was studied.

3.2. Factors affecting hydraulic properties variations

3.2.1. Original porosity

In general, at the same water pressure and particle size composition, the sample with higher original porosity obtains a higher permeability and porosity when the test is completed (see results for samples 1, 2 and 3 in Figs. 7 and 8(a)). Also, during the rearrangement of large fragments at the first phase of the tests it is observed that the higher the original porosity is, the bigger the rate of porosity change is (see Fig. 8(b)). Moreover, Fig. 7 shows that, from sample 1 to samples 2 and 3, as the original porosity of the sample increases the required time for the adjustment of large rock fragments decreases. In addition, it is observed that with the increase of original porosity, the

durations of water inrush stage (phase two), and moderate particle seepage stage (phase three) increase and decrease, respectively (see Fig. 7).

3.2.2. Particle size composition

As the results of tests on samples 4, 5 and 6 show (see Figs. 7 and 8(a)), generally, at the same original porosity and water pressure, the sample with higher percentage of small particles (particles smaller than 10mm in size), reaches higher permeability and porosity on the completion of the test. Also, based on the results it is evident that during the first phase of the tests, higher percentage of small particles in the sample would result in higher rate of porosity change (see Fig. 8(b)). This is because in a sample with significantly more small particles at the initial state (e.g., sample 6) there is a higher potential for particle discharge, and hence a rapid permeability and porosity change.

Furthermore, comparing the results of tests over samples 4, 5 and 6 (see Fig. 7), it can be seen that as the amount of small particles in the samples increases, the adjustment of the large rock fragments (i.e., phase one) occurs more rapidly. Meanwhile, a clear increase in the duration of water inrush phase, during which substantial amount of small particles are washed away, has been witnessed. That coincides with an increased quantity of particles discharged out of the samples during phase two of permeability evolution, which could be expected given the increasing proportion of small particles in the original formation of samples. However, it is an interesting observation considering the lower original porosity and permeability in samples with higher amount of small particles. Subsequently, with the increase of small particles contribution in the original sample preparations (i.e., from sample 4 to 6) the duration of phase three, when steady seepage happens, is shortened.

3.2.3. Water pressure

The tests results for samples 7, 8 and 9, in Figs. 7 and 8, show that at the same original porosity and particle size composition, if the water flow pressure increases, the sample will obtain higher

values of permeability and porosity upon the completion of the tests. During the first phase of the tests when the particles are being rearranged, with higher applied water pressure, the rate of the porosity change will be higher. This is mainly because water flow with higher pressure has higher particle flushing ability. However, it could be observed from Figs. 7 and 8 that overall for a 4MPa increase of applied water flow pressure the durations of different phases (e.g., phases 1 and 2) have changed rather moderately.

An overall observation from the tests is that the samples with higher original porosity and more small particles, that is under a higher flow pressure, will obtain higher permeability and porosity values under the water inrush. Also, the rate of porosity increase is found to be significantly higher during phase one of the tests when the large rock fragments are being rearranged. Moreover, the effect of all factors influencing hydraulic properties variations can be summed up in the migration of small particles.

3.3. Predictive models for permeability and porosity evolution

There are not many reported field measurements for permeability evolution of granular rocks deep under the ground, mainly due to their inaccessibility to carry out direct measurements. It is therefore common practice to predict porosity and permeability using limited experimental data. A number of models have been developed for calculating the hydraulic permeability κ of an aggregated medium. In Table 2, the most commonly used models for the evaluation of permeability are summarized. Based on these models, the corresponding permeability evolution functions for κ_j/κ_0 (where κ_0 and κ_j are the original permeability value and the permeability at time j , respectively) have been obtained (as listed in Table 2).

As shown in Table 2, to use the predictive models it is necessary to determine the values of effective particle size $d_j^e(d_j^{10})$, d_j^{20} and mean particle size $d_j^m(d_j^{50})$ of the samples. For all samples

of this work $d_j^0 = 2.5\text{mm}$ and $d_j^{100} = 20\text{mm}$, at any time. Because the diameters of the washed away particles (with total collected mass of m_j) at any time interval are within the range $2.5\text{ mm} < d_{m_j} < 10\text{ mm}$, therefore the percentage for 2.5~10 mm size particles remaining within the sample at any time can be determined from $\bar{d} = \frac{m_{10} - m_j}{m_s - m_j}$, and subsequently the remaining percentage for 2.5~15 mm particles can be determined by $\bar{\bar{d}} = \frac{m_{15} - m_j}{m_s - m_j}$. In these equations, m_{10} represents the original mass for particles of size 2.5–5 mm and 5–10 mm before water flow, and m_{15} represents the original mass for particles of size 2.5–5 mm, 5–10 mm and 10–15 mm before water flow. Therefore, we can determine the particle size distribution of each sample at any time during the test d_j^k ($0 \leq k \leq 100$) by:

$$d_j^k = \begin{cases} 2.5 + \frac{(10 - 2.5) \times k}{\bar{d}} & (0 \leq k \leq \bar{d}) \\ 10 + \frac{(15 - 10) \times (k - \bar{d})}{\bar{\bar{d}} - \bar{d}} & (\bar{d} < k \leq \bar{\bar{d}}) \\ 15 + \frac{(20 - 15) \times (k - \bar{\bar{d}})}{100 - \bar{\bar{d}}} & (\bar{\bar{d}} < k \leq 100) \end{cases} \quad (15)$$

For example, for all samples the particle size distribution plots at the end of the test (after 160 seconds) and the variations of d_j^e (d_j^{10}) are shown in Figs. 9 and 10, respectively.

Using the approach described above, the necessary data to use for the permeability evolution models (see Table 2) are obtained and used for the evaluation of their performances over the test data. As an example, Fig. 11 shows the predictions of permeability evolution over the test samples obtained from using Carman–Kozeny model. As an example, the data corresponding to the analysis of the permeability evolution for a sample test is summarized in Table 3. In order to compare the performances of the predictive models for permeability (or porosity) evolution, a simple statistical efficiency criterion, based on coefficient of determination factor R^2 , is used

$$R^2 = \frac{\sum_{j=1}^n (\kappa_j^m)^2 - \sum_{j=1}^n (\kappa_j^m - \kappa_j^p)^2}{\sum_{j=1}^n (\kappa_j^m)^2} \quad (16)$$

where n is the total number of test data; κ_j^m is the experimentally measured value, and κ_j^p is the model prediction associated with a test. The results of R^2 values for different models and test samples are drawn in Fig. 12.

As shown in Fig. 11, using a predictive model the calculated permeabilities are almost always higher than those obtained from the tests. This could indicate that during the tests perhaps not all of the fractures contributed in the flow, and parts of the fracture network were ineffective in the small particle migration. However, given the generally high values of R^2 (Fig. 12), it appears that the application of effective porosity (fracture) in flow for the prediction of permeability variations can yield sufficiently accurate results.

Comparing the model predictions for permeability variations of samples 1, 2 and 3 in Fig. 12, it is observed that for sample 1 the highest average R^2 is achieved (i.e., 0.9837). This could be mainly because the sample with less original porosity, which means less inherent original fracture, would have less ineffective flow channels. Furthermore, from the same figure, comparing the model predictions over the test results from samples 4, 5 and 6, it is observed that the lowest average R^2 value is obtained for sample 6 (i.e., 0.9202). This indicates that the sample with fewer small particles, i.e., more large rock fragments hence farther fracture network, would have more ineffective fractures. A comparison of the prediction results corresponding to samples 7, 8 and 9 shows that the average value R^2 for sample 9 is the least, which means higher water pressure causes more fractures in the sample. In summary, it is concluded that the accuracy of permeability (porosity) evolution models is higher for the sample with less original porosity, more small particles and subjected to lower water pressure.

Furthermore, Fig. 12 shows that the average R^2 value from Hazen equation is the lowest (i.e., 0.9043) among the others. Its prediction performance using the data from sample 6 is the poorest

with an R^2 value of 0.7557. Apart from the Hazen equation, the R^2 values from other models are all larger than 0.93, indicating a high level of accuracy. The average R^2 values from the application of Happel, Zamarin and Carman–Kozeny equations are greater than 0.98, which indicate remarkable prediction performance. Particularly in case of Carman–Kozeny equation, the predictions are very close to the measured permeabilities (with an R^2 value of almost 0.99).

4. Conclusions

The fault fracture zones, which contain substantial amounts of granular rocks, can act as major water outburst channels. Therefore, the geological composition or type of rock composing the existing faults could be the crucial factor in determining the safety of coal mines with underlying aquifers. To study the mechanism of effect of mining on water inrush within faults that is caused by small particle migration, a rock testing system has been designed and constructed to conduct a series of tests for evaluating the hydraulic properties of granular sandstones. The permeability and porosity changes in granular rock samples under varying original porosity, particle size composition and water pressure were studied.

According to the experimental observations, during the tests the permeability and porosity increased with time until they reached to a peak value. The overall permeability evolution during the tests could be divided into four different stages. In the first stage, the permeability increased gradually with almost no apparent migration of small particles, the water inflow was slightly turbid, and the porosity increase rates were at their maximum. In the second stage, the water inflow velocity increased rapidly in a very short time; furthermore, major channels for water flow and particle migration were formed resulting in the erosion of maximum amounts of small particles out of the samples. During the third phase, moderate amounts of small particles continued migrating out of the samples through the major flow channels which were formed in the previous stage; hence, the permeability and porosity increased only slowly in this phase. In the final stable water flow stage,

there were not any noticeable amount of small particles migrating out of the samples and therefore the permeability values became constant.

The fluctuations of permeability-time relationship were mainly observed in the first two phases. This was deemed to be due to the crushing of corners and edges of the larger particles and their rearrangements that resulted in the development of new and temporary fracture channels within the samples. It can be concluded that when mining excavations are carried out, the redistribution of the stress field leads to the reactivation of faults that consequently result in the increase of permeability within the crushed zones of the existing faults. Hence, potential flow channels for water inrush are generated within the damaged zones of the faults. Furthermore, the erosion of small particles under high water pressure could tabulate different seepage mechanisms (e.g., pore flow, fissure flow and pipe flow), which in turn result in greater probability of groundwater inrush incidents. With higher original porosity, particle sizes and water flow pressures, the duration of the water inrush and stable seepage phases decreases more quickly. This is due to the fact that the higher those attributes are, the greater the influence of small particle migration will be on the variations of the hydraulic properties.

A number of empirical equations (Table 2) for calculating the hydraulic permeability of an aggregated medium were used to model the porosity-permeability relationship evolution under the effect of small particle migration. The prediction of permeability (and porosity) evolutions indicated that not all of the fracture structures were effective channels for particle flow, and parts of the fracture network were not contributing in the particle migration. In summary, the sample with less original porosity, more small particles and under lower water pressure would have smaller fracture network and hence fewer ineffective flow channels. Therefore, under these conditions the accuracy of the predictive models for permeability (and porosity) evolution would be higher.

Acknowledgments

This work was supported by the Fundamental Research Funds for the Central Universities (2015XKZD06) and the Innovative Research Group of the National Natural Science Foundation of China (51421003).

References

- Babiker, M., Gudmundsson, A., 2004. The effects of dykes and faults on groundwater flow in an arid land: the Red Sea Hills, Sudan. *Journal of Hydrology* 297(1-4), 256–273
- Bai, H.B., Ma, D., Chen, Z.Q., 2013. Mechanical behavior of groundwater seepage in karst collapse pillars. *Engineering Geology*, 164, 101-106.
- Bai, H.B., Miao, X.X., 2016. Hydrogeological characteristics and mine water inrush prevention of late Paleozoic coalfields. *Journal of China University of Mining and Technology*. 45(1), 1-10.
- Blodgett, S., Kuipers, J.R., 2002. *Underground hard-rock mining: subsidence and hydrologic environmental impacts*. Bozeman, MT: Centre of Science in Public Participation.
- Booth, C.J., 2006. Groundwater as an environmental constraint of longwall coal mining, *Environmental Geology*, 49 (6), 796-803.
- Buliangou Geological and Mineral Resource Exploration (BGMRE), 2006. Buliangou coal area of Zhungeer coalfield. Inner Mongolia Mengtai Buliangou Coal Industry Co. Ltd, Eerduosi.
- Caine, J.S., Evans, J.P., Foster, C.B., 1996. Fault zone architecture and permeability structure. *Geology* 24(11), 1025–1028
- Huang, Z., Jiang, Z.Q., Zhu, S.Y., Wu, X.S., Yang, L.N., Guan, Y.Z., 2016. Influence of structure and water pressure on the hydraulic conductivity of the rock mass around underground excavations. *Engineering Geology*, 202 (4), 74-84.

- Johnsen, Ø., Chevalier, C., Lindner, A., Toussaint, R., Clément, E., Måløy, K.J., Flekkøy, E.G., Schmittbuhl, J., 2008. Decompaction and fluidization of a saturated and confined granular medium by injection of a viscous liquid or a gas. *Physical Review E, American Physical Society*, 78, 051302.
- Johnsen, Ø., Toussaint, R., Måløy, K.J., Flekkøy, E.G., Schmittbuhl, J., 2007. Coupled air/granular flow in a linear Hele-Shaw cell, *Physical Review E, American Physical Society*, 77, 011301.
- Lee, D.J., Chen, G.W., Liao, Y.C., Hsieh, C.C., 1996. On the free-settling test for estimating activated sludge floc density. *Water Research*, 30(3), 541–550.
- Li, X.Y., Logan, B.E., 1997. Collision frequencies of fractal aggregates with small particles by differential sedimentation. *Environmental Science and Technology*, 31(4), 1229–1236.
- Li, G.C., Jiang, Z.H., Lv, C.X., Huang, C., Chen, G., Li, M.Y., 2015. Instability mechanism and control technology of soft rock roadway affected by mining and high confined waters. *International Journal of Mining Science and Technology*. 25(4), 573–580.
- Li, G.Y., Zhou, W.F., 2006. Impact of karst water on coal mining in North China. *Environmental Geology* 49, 449-57.
- Li, L.C., Yang, T.H., Liang, Z.Z., Zhu, W.C., Tang, C.A., 2011. Numerical investigation of groundwater outbursts near faults in underground coal mines. *International Journal of Coal Geology*, 85(3-4), 276–288
- Lu, H.F., Yao, D.X., Shen, D., Cao, J.Y., 2015. Fracture mechanics solution of confined water progressive intrusion height of mining fracture floor. *International Journal of Mining Science and Technology*. 25(1), 99–106.

- Lu, Y.L., Wang, L.G., 2015. Numerical simulation of mining-induced fracture evolution and water flow in coal seam floor above a confined aquifer. *Computers and Geotechnics* 67, 157–171
- Ma, D., Bai, H.B., Chen, Z.Q., Pu, H., 2015b. Effect of particle mixture on seepage properties of crushed mudstones, *Transport in Porous Media*, 108(2), 257–277.
- Ma, D., Bai, H.B., Miao, X.X., Pu, H., Jiang, B.Y., Chen, Z.Q., 2016b. Compaction and seepage properties of crushed limestone particle mixture: an experimental investigation for Ordovician karst collapse pillar groundwater inrush, *Environmental Earth Sciences*, 75, 11.
- Ma, D., Bai, H.B., Wang, Y.M., 2015a. Mechanical behavior of a coal seam penetrated by a karst collapse pillar: mining induced groundwater inrush risk, *Natural Hazards*, 75(3), 2137–2151.
- Ma, D., Miao, X.X., Bai, H.B., Huang, J.H., Pu, H., Wu, Y., Zhang, G.M., Li, J.W., 2016a. Effect of mining on shear sidewall groundwater inrush hazard caused by seepage instability of the penetrated karst collapse pillar. *Natural Hazards*, 82(1), 73-93.
- Meng, Z.P., Shi, X.C., Li, G.Q., 2016. Deformation, failure and permeability of coal-bearing strata during longwall mining. *Engineering Geology*, 208(24), 69–80.
- Miao, X.X., Cui, X.M., Wang, J.A., Xu, J.L., 2011a. The height of fractured water-conducting zone in undermined rock strata. *Engineering Geology*, 120, 32–39.
- Miao, X.X., Li, S.C., Chen, Z.Q., Liu, W.Q., 2011b. Experimental study of seepage properties of broken sandstone under different porosities. *Transport in Porous Media*, 86, 805–814.
- Miao, X.X., Liu, W.Q., Chen, Z.Q., 2004. *Seepage Theory of Mining Strata*. Science Press, Beijing.
- Miao, X.X., Qian, M.G., 2009. Research on the green mining of coal resources in China: current status and future prospects. *Journal of Mining and Safety Engineering*, 26(1), 1-14.

- Niebling, M., Toussaint, R., Flekkøy, E.G., Måløy, K.J., 2012. Dynamic aero fracture of dense granular packings, *Physical Review E*, American Physical Society, 86, 061315.
- Rogak, S.N., Flagan, R.C., 1990. Stokes drag on self-similar clusters of spheres. *Journal of Colloid and Interface Science*, 134(1), 206–218.
- Rutter, E.H., Hackston, A.J., Yeatman, E., Brodie, K.H., Mecklenburgh, J., May, S.E., 2013. Reduction of friction on geological faults by weak-phase smearing. *Journal of Structural Geology*, 51, 52-60.
- State Administration of Coal Mine Safety, 2014. Analysis on China's coal mine accidents in 2013. Accident Investigation Division of State Administration of Coal Mine Safety, Beijing.
- Sun, W.J., Zhou, W.F., Jiao, J., 2016. Hydrogeological classification and water inrush accidents in China's coal mines, *Mine Water and the Environment*, 35(2), 214-220.
- Veerapaneni, S., Wiesner, M.R., 1996. Hydrodynamics of fractal aggregates with radially varying permeability. *Journal of Colloid and Interface Science*, 177(1), 45–57.
- Vukovic, M., Soro, A., 1992. Determination of hydraulic conductivity of porous media from grain-size composition: Water Resources Publications, Littleton, CO, 83.
- Wu, Q., Zhou, W.F., 2008. Prediction of groundwater inrush into coal mines from aquifers underlying the coal seams in China: vulnerability index method and its construction. *Environmental Geology*, 56, 245–254.
- Zhang, B.Y., Bai, H.B., Zhang, K., 2016. Seepage characteristics of collapse column fillings. *International Journal of Mining Science and Technology*, 26 (2), 333–338
- Zhang, R., Jiang Z.Q., Zhou, H.Y., Yang, C.W., Xiao, S.J., 2014. Groundwater outbursts from faults above a confined aquifer in the coal mining, *Natural Hazards*, 71(3), 1861-1872

Zhu, S.Y., Jiang, Z.Q., Cao, D.T., Sun, Q., Yang, C.W., 2013. Restriction function of lithology and its composite structure to deformation and failure of mining coal seam floor. *Natural Hazards*, 68(2), 483-495

Zhu, W.C., Wei, C.H., 2011. Numerical simulation on mining-induced water inrushes related to geologic structures using a damage-based hydromechanical model. *Environmental Earth Sciences* 62, 43–54.

ACCEPTED MANUSCRIPT

Figure and Table Captions List

Fig. 1 Mining-induced small particle migration in faults above confined aquifer

Fig. 2 Schematics of particle migration testing system

Fig. 3 The detail components of the rock granules flow apparatus. (a) connection principle; (b) porous plate; (c) water flushing cap; (d) outflow regulator. Note: 1–loading plate; 2–overflow tank cover; 3–overflow tank; 4–outlet pipe; 5,12–bolts; 6–cylindrical sample container; 7–O-shaped rubber seal rings; 8 –pedestal; 9–porous metal disk; 10–filter pad; 11–sample; 13–water flushing cap; 14–outflow regulator.

Fig. 4 Picture of rock skeleton mixed with small rock particles from a fault

Fig. 5 Sandstone test sample with particle of about 15–20 mm

Fig. 6 Illustration of the different heights involved in calculating the permeability. Note: h_s –height of granular sandstone sample; H_1 – height of cylindrical tube/container; H_2 –base plate thickness; H_3 –porous plate thickness; H_4 – filtration pad thickness; H_5 –flow piston thickness; H_6 –height of the overflow tank head in the cylindrical tube, H_7 –overflow tank height; H_8 –height of the overflow tank head that exceeds the cylindrical tube.

Fig. 7 The variations of permeability with time for different samples

Fig. 8 The variations of (a) porosity, and (b) porosity increase rate with time for different samples

Fig. 9 Particle size distribution for each sample at the end of the tests

Fig. 10 The variations of $d_j^e (d_j^{10})$ for each sample during the tests

Fig. 11 Measured and predicted values for permeability – porosity relationship using Carman–Kozeny model

Fig. 12 R^2 values for model predictions of permeability evolution for different samples

Table 1 Details of testing samples

Table 2 Correlation of the permeability and porosity

Table 3 Model prediction parameters used in Carman–Kozeny equation for sample 6

ACCEPTED MANUSCRIPT

Table 1 Details of testing samples

Sample No.	Total mass (g)	Sample height (mm)	Original porosity	Particle size weight ratio	Mass contribution of each particle size range (g)				Water pressure (MPa)
					0–5 mm	5–10 mm	10–15 mm	15–20 mm	
1	1800	110	0.288	1:1:1:1	450	450	450	450	0.7
2,5,8		120	0.348		450	450	450	450	
3		130	0.398		450	450	450	450	
4		120	0.348	1:1:2:2	300	300	600	600	
6				2:2:1:1	600	600	300	300	
7				1:1:1:1	450	450	450	450	0.3
9					450	450	450	450	1

Table 2 Correlation of the permeability and porosity

Correlation	Permeability function κ_j	κ_j/κ_0
Hazen (Vukovis and Soro 1992)	$\frac{\mu_w}{\gamma_w} [400 + 40(\phi_j - 26)] (d_j^{20})^2$	$\left(\frac{d_j^{20}}{d_0^{20}}\right)^2 \frac{[400 + 40(\phi_j - 26)]}{[400 + 40(\phi_0 - 26)]}$
Kruger (Vukovis and Soro 1992)	$240 \frac{\mu_w}{\gamma_w} (d_j^e)^2 \frac{\phi_j}{(1-\phi_j)^2}$	$\left(\frac{d_j^e}{d_0^e}\right)^2 \left(\frac{\phi_j}{\phi_0}\right) \left(\frac{1-\phi_0}{1-\phi_j}\right)^2$
Brinkman (Lee et al., 1996; Li and Logan, 1997)	$\frac{(d_j^m)^2}{72} \left(3 + \frac{3}{1-\phi_j} - 3\sqrt{\frac{8}{1-\phi_j} - 3}\right)$	$\left(\frac{d_j^m}{d_0^m}\right)^2 \frac{3 + \frac{3}{1-\phi_j} - 3\sqrt{\frac{8}{1-\phi_j} - 3}}{3 + \frac{3}{1-\phi_0} - 3\sqrt{\frac{8}{1-\phi_0} - 3}}$
Happel (Veerapaneni and Wiesner, 1996)	$\frac{(d_j^m)^2}{18} \frac{3 - 4.5\xi_j + 4.5\xi_j^5 - 3\xi_j^6}{\xi_j^3(3 + 2\xi_j^5)}$ $\xi_j = (1-\phi_j)^{1/3}$	$\left(\frac{d_j^m}{d_0^m}\right)^2 \frac{\xi_0^3(3 + 2\xi_0^5)(3 - 4.5\xi_j + 4.5\xi_j^5 - 3\xi_j^6)}{\xi_j^3(3 + 2\xi_j^5)(3 - 4.5\xi_0 + 4.5\xi_0^5 - 3\xi_0^6)}$ $\xi_j = (1-\phi_j)^{1/3}$
Zamarin (Vukovis and Soro 1992)	$8.07 \frac{\mu_w}{\gamma_w} (d_j^e)^2 \left(\frac{1.275 - 1.5\phi_j}{1-\phi_j}\right)^2 \phi_j^3$	$\left(\frac{d_j^e}{d_0^e}\right)^2 \left[\frac{(1-\phi_0)(1.275 - 1.5\phi_j)}{(1-\phi_j)(1.275 - 1.5\phi_0)}\right]^2 \left(\frac{\phi_j}{\phi_0}\right)^3$
Carman-Kozeny (Rogak and Flagan, 1990; Lee et al., 1996)	$\frac{(d_j^m)^2}{180} \frac{\phi_j^3}{(1-\phi_j)^2}$	$\left(\frac{d_j^m}{d_0^m}\right)^2 \left(\frac{1-\phi_0}{1-\phi_j}\right)^2 \left(\frac{\phi_j}{\phi_0}\right)^3$

Table 3 Model prediction parameters used in Carman–Kozeny equation for sample 6

Time j	0	20	40	60	80	100	120	140	160
$d_j^m (d_j^{50})$	8.125	8.297	8.437	8.477	8.491	8.499	8.508	8.508	8.508
ϕ_j	0.348	0.384	0.410	0.417	0.419	0.420	0.421	0.422	0.422
κ_j (measured)	27.554	40.797	49.188	55.735	59.073	61.875	62.673	62.774	62.774
κ_j (predicted)	27.480	43.372	59.196	64.214	65.978	67.039	68.188	68.212	68.212

Figure 1

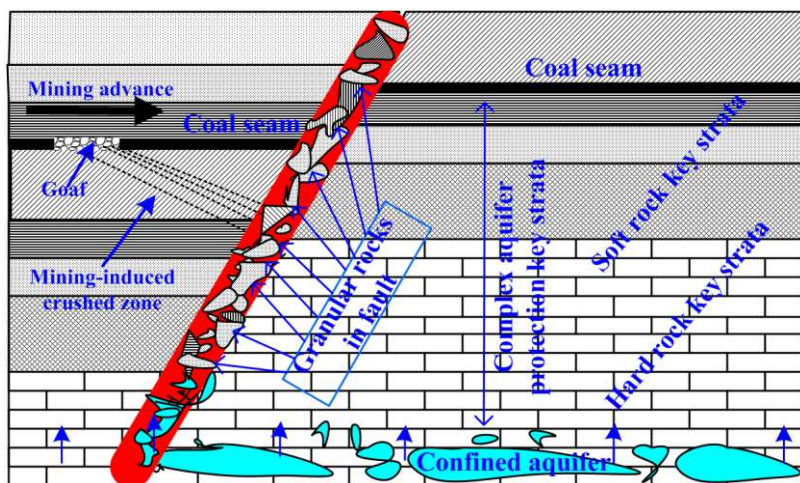


Figure 2

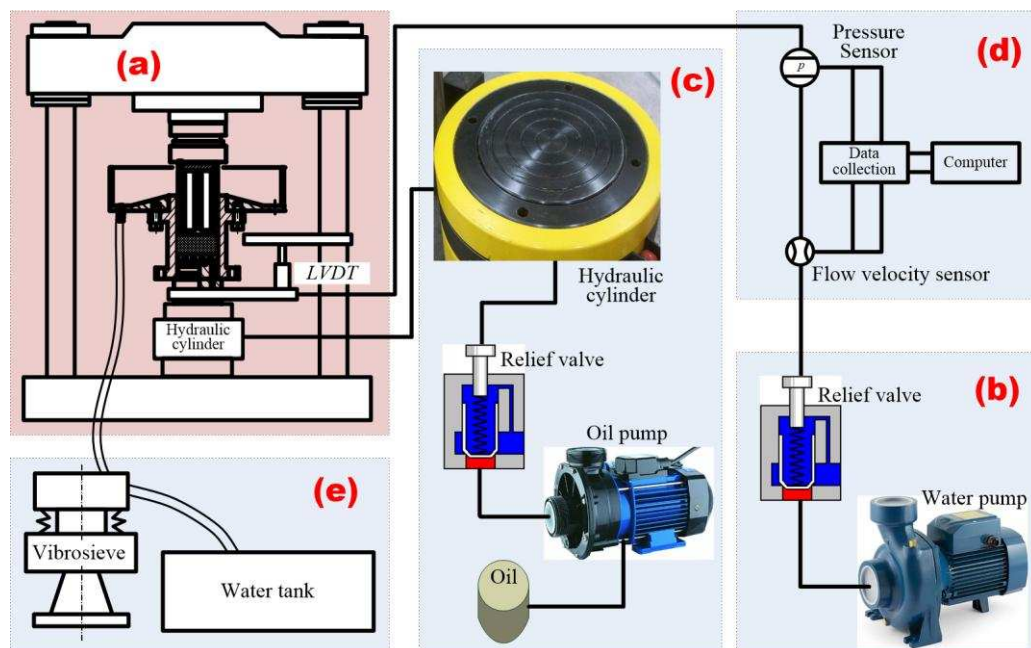


Figure 3

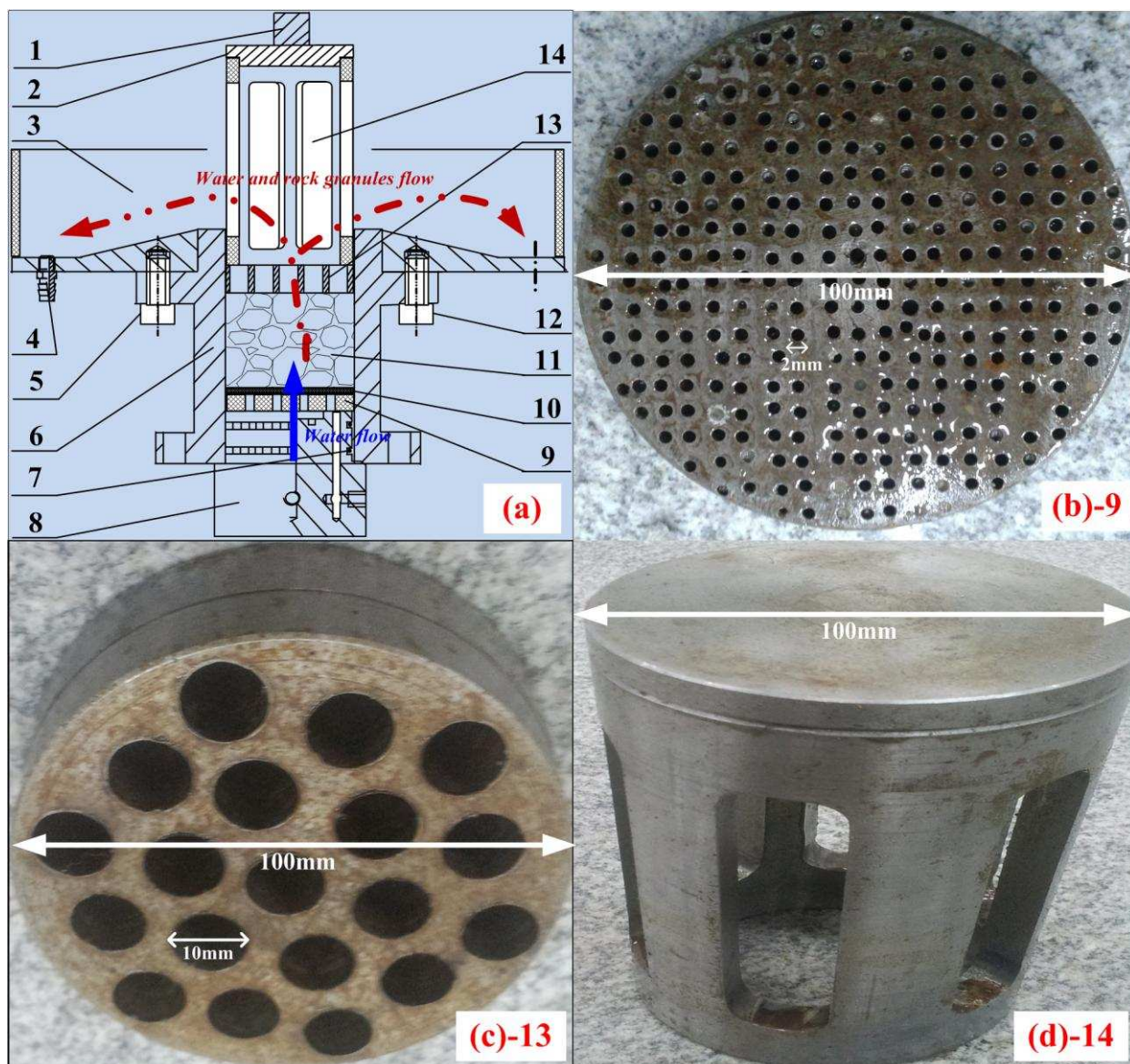


Figure 4

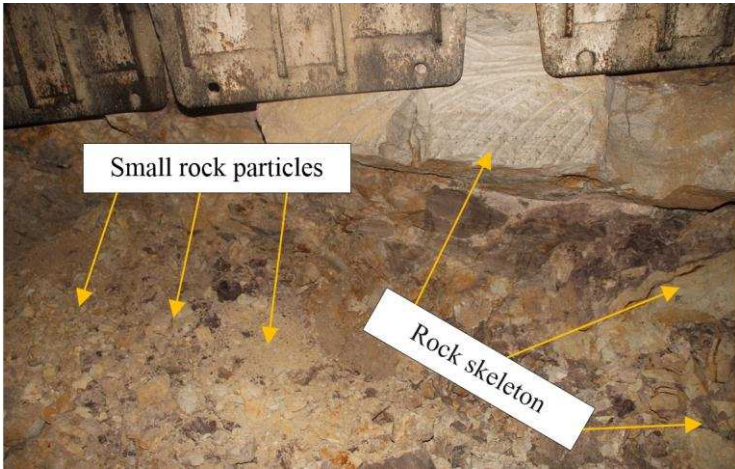
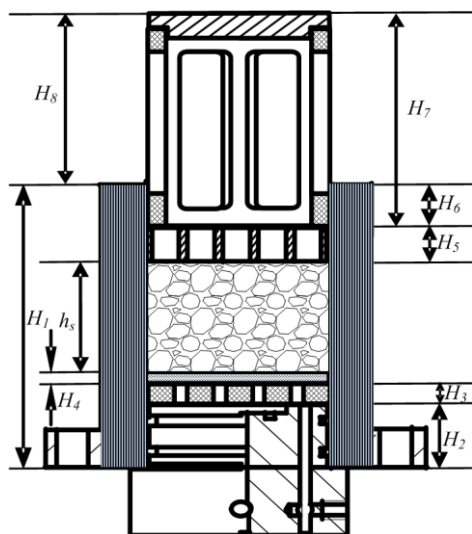


Figure 5



ACCE

Figure 6



ACCEPTED MANUSCRIPT

Figure 7

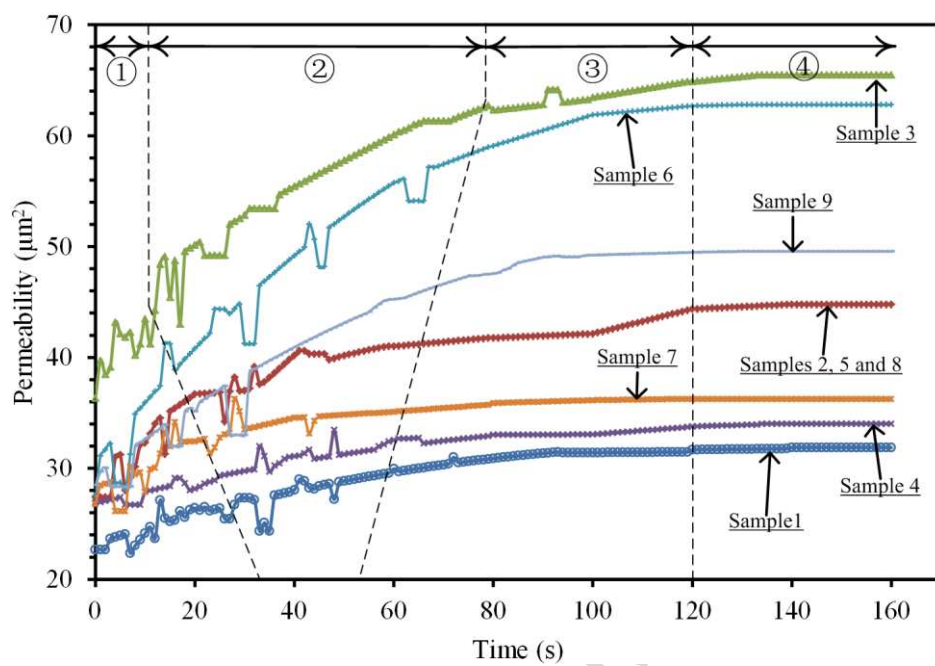


Figure 8a

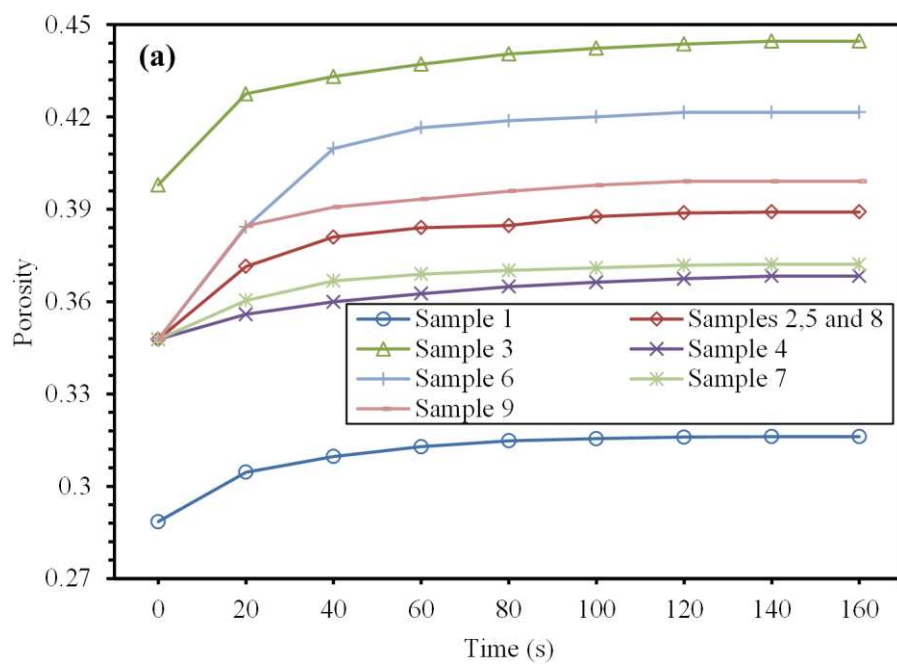


Figure 8b

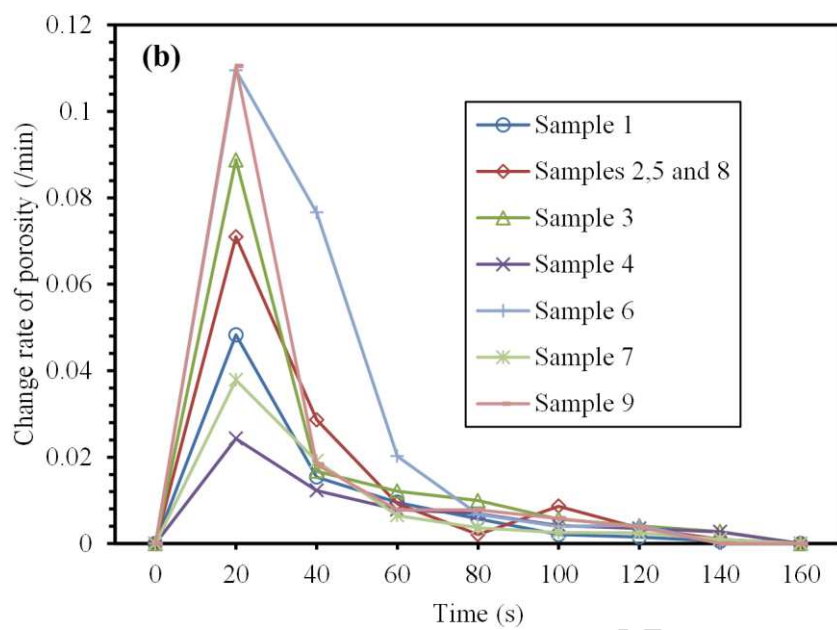


Figure 9

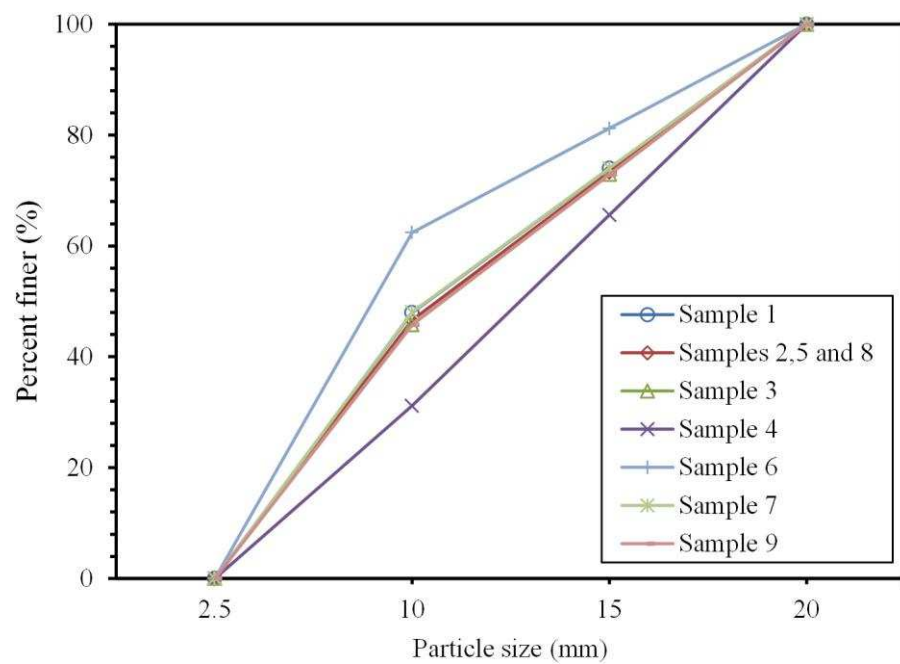


Figure 10

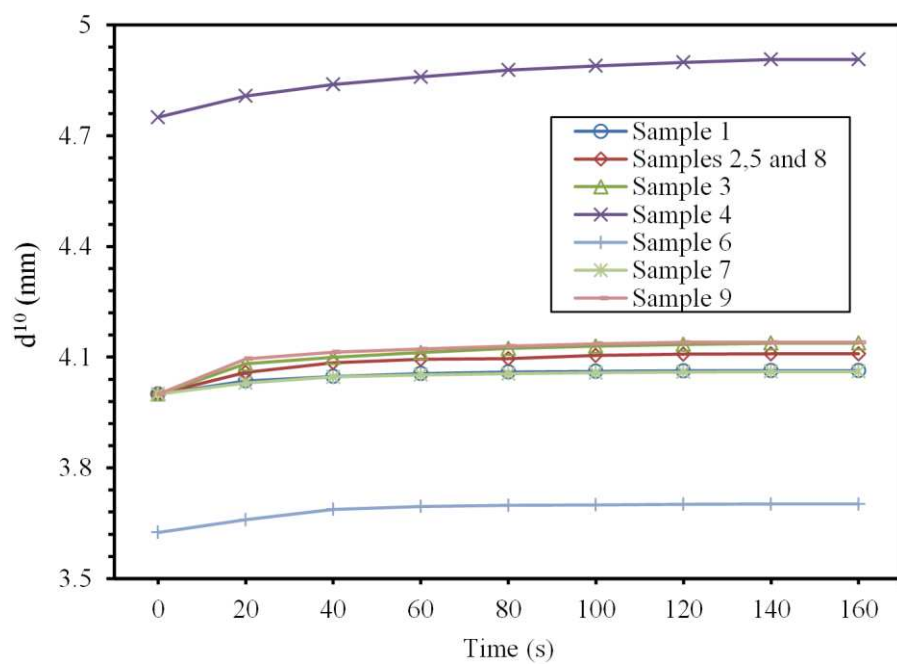


Figure 11

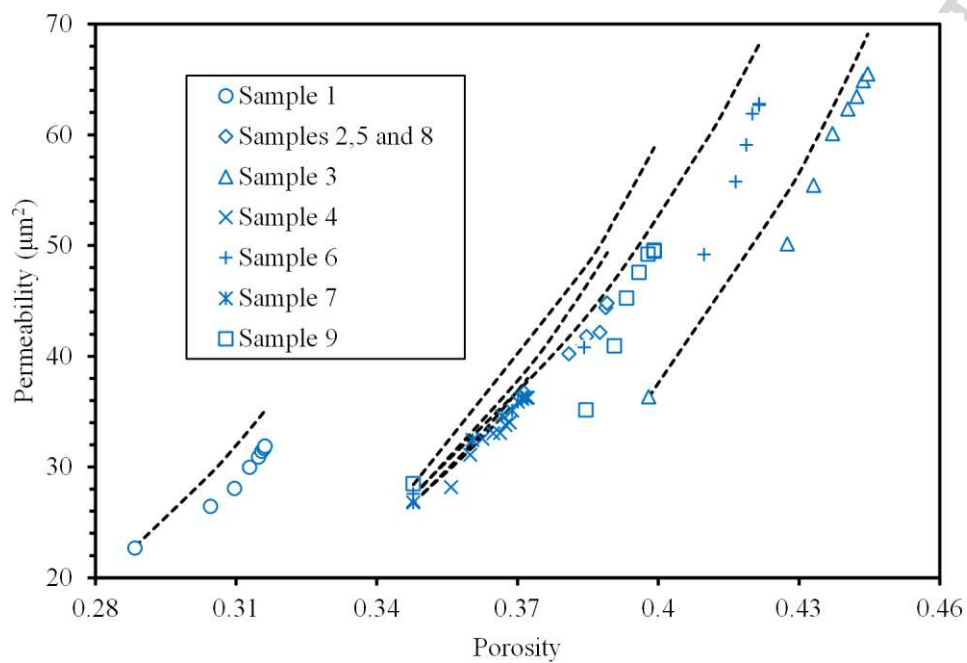
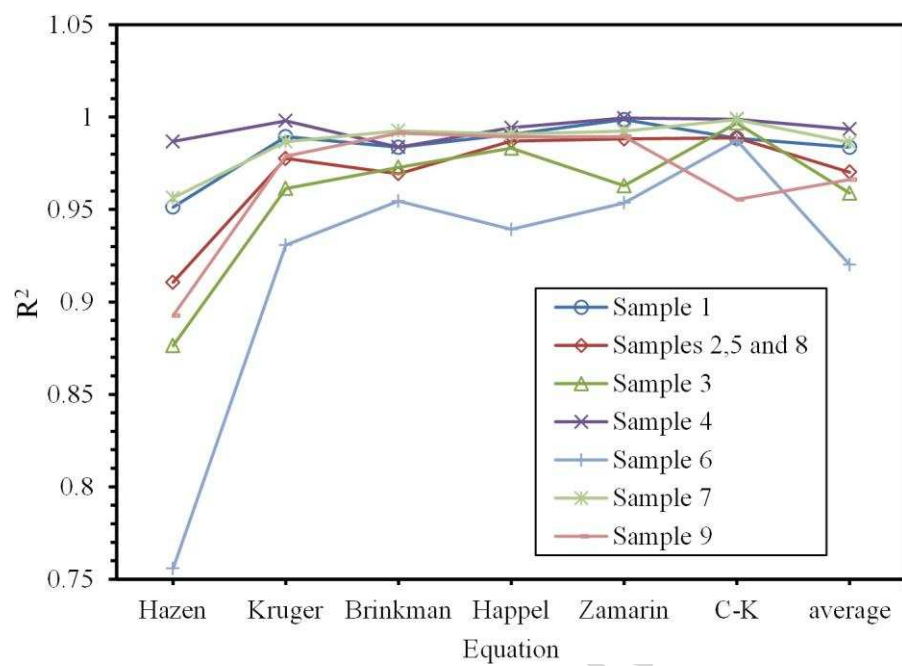


Figure 12



Highlights

- The permeability evolution within granular sandstones under water inrush can be divided into four different phases.
- Particle migration has an essential effect on permeability increase during water inrush.
- Parts of the fracture network within the granular media are not effective for water and particle flow.